Pore geometry as a control on rock strength

A. Bubeck[1,2], R.J. Walker[1], D. Healy[3], M. Dobbs[4], D.A. Holwell[1]

[1] *Department of Geology, University of Leicester, Leicester, UK*

[2] *School of Earth and Ocean Sciences, Cardiff University, Cardiff, UK*

[3] *School of Geosciences, King's College, University of Aberdeen, Aberdeen, UK*

[4] *Rock Mechanics and Physics Laboratory, British Geological Survey, Keyworth, Nottingham, UK*

ABSTRACT

The strength of rocks in the subsurface is critically important across the geosciences, with implications for fluid flow, mineralization, seismicity, and the deep biosphere. Most studies of porous rock strength consider the scalar quantity of porosity, in which strength shows a broadly inverse relationship with total porosity, but pore shape is not explicitly defined. Here we use a combination of uniaxial compressive strength measurements of isotropic and anisotropic porous lava samples, and numerical modelling to consider the influence of pore shape on rock strength. Micro computed tomography (CT) shows that pores range from sub-spherical to elongate and flat ellipsoids. Samples that contain flat pores are weaker if compression is applied parallel to the short axis (i.e. across the minimum curvature), compared to compression applied parallel to the long axis (i.e. across the maximum curvature). Numerical models for elliptical pores show that compression applied across the minimum curvature results in relatively broad amplification of stress, compared to compression applied across the maximum curvature. Certain pore shapes may be relatively stable and remain open in the upper crust under a given remote stress field, while others are inherently weak. Quantifying the shape, orientations, and statistical distributions of pores is therefore a critical step in strength testing of rocks.

1. INTRODUCTION

Numerical and experimental studies of strength across material sciences, biomechanics, and geology, show a strong link between porosity and strength in both natural and manufactured porous materials: an increase in porosity or pore size is typically associated with a decrease in brittle strength and fracture toughness (Figure 1A: Rice, 1998; Leguillon and Piat, 2008; Schaefer et al., 2015). Figure 1 shows that although there is a broad inverse relationship between strength and porosity, but strength ranges substantially for a given porosity. Notably, it is typical for studies of the strength of porous rocks to tacitly assume isotropic pore shape. The mechanical response of rocks that exhibit foliations (e.g., bedding, banding, or fractures) is strongly controlled by the relative orientation of the applied load and foliation plane (i.e. the β-angle: e.g. Paterson and Wong, 2005). In the case of fractures, which are often modelled as penny-shaped cracks (i.e. oblate ellipsoidal pores, with semi-axes a=b>>c), the aspect ratio (which we define here as c/a, such that a low aspect ratio approaches a sphere with value 1, and a high aspect ratio approaches 0) is so high (<< 0.1) that compression applied to the short axis facilitates elastic closure and strengthening; compression parallel (or at a low angle) to the crack long axes promotes opening and weakening (e.g. Sibson, 1985). Rocks can also contain prolate to oblate pores with aspect ratios between those of spherical pores and planar discontinuities (i.e. aspect ratio in the range 0.1-1.0). In such cases, elastic closure of the short axis dimension is not possible for most rocks, and the mechanical response should be expected to differ from rocks containing penny shaped cracks. Pore geometry, and the resulting mechanical influence, is poorly documented in studies of rock strength. Here we use physical and mechanical characterization of minimally weathered, 750-1500 year old olivine-tholeiite lava (henceforth, *basalt* lava) from the south flank of Kilauea Volcano, Hawai'i, to constrain the effect of low aspect ratio pores (i.e., vesicles with aspect ratios >0.1) on rock strength, through a combination of Uniaxial Compressive Strength (UCS) tests, and numerical modelling. We show that pore geometry – not just the scalar quantity of porosity – provides a fundamental control on rock strength. Therefore, unless pore geometry is well

characterized and the effective bulk orientation of the pores are known with respect to the principal stress axes, mechanical test results are not directly comparable.

2. Background and Methods

2.1 Kilauea Pahoehoe Lava

Small volume tholeiitic pahoehoe lavas are emplaced as non-channelized, inflated sheets on the subhorizontal (1-2°) south flank of Kilauea Volcano. Sheet flows have been observed as thin layers (10-50 cm thick), inflating to thicknesses as great as 4 m (e.g. Hon et al., 1994). Samples were collected from exposed lavas along open portions of the ENE-WSW striking Kulanaokuaiki fault, located at the eastern end of the Koa'e fault system, 7-8 km south of Kilauea's summit caldera (Figure 2). Normal faults in the Koa'e system develop at shallow depths (<5 km: e.g. Lin and Okubo, 2016) with the early stages of fault propagation associated with the opening of extension fractures that reactivate pre-existing cooling joints, where observed in the near surface (e.g., Duffield, 1975). The Kulanaokuaiki fault accommodates 0 to 15 m of displacement (Duffield, 1975), and was most recently active during the December 1965 eruption of Kilauea. Careful characterisation of several lavas exposed in the fault footwall reveals a distinctive 3-zone physical stratigraphy based on the total volume and geometry of vesicles and the scale of joint patterns: (1) a top of 18-31% porosity, with sub-spherical vesicles up to 4 mm in diameter; (2) a core of 12-13% porosity, with sub-spherical vesicles up to 1.5 mm in diameter; and (3) a base, of 15-19% porosity, with oblate or amalgamated vesicles up to 15 mm in diameter. The thickness of these three zones scale proportionally with the thickness of a lava, and representative samples were targeted for each zone. Basalt lava samples for this study are fine grained with porphyritic texture; phenocrysts are dominantly of olivine and plagioclase, set in a matrix of granular plagioclase and pyroxene. Olivine phenocrysts are typically euhedral up to 1.00-1.25 mm in size.

Field and hand sample observations show that oblate vesicles in the basal zone are aligned sub-horizontally, parallel to bedding; in the lava core and top zones, the minor fraction of non-spherical vesicles appear to be randomly oriented. Sample porosity was obtained for samples from each zone, using the saturation and calliper method, following the International Society for Rock Mechanics (ISRM) suggested methodology (Bieniawski and Bernede, 1979a).

2.2. CT and volume analysis

Lava samples were analysed using a Nikon XT225 Metris X-ray computed tomography (X-ray CT) scanner to determine total porosity, and pore shape. Sample cores were imaged via a series of X-ray slices resulting in ~3000 images collected at 0.12° increments in a 360° rotation. The X-ray beam attenuates in a known way with material density (e.g., Roche et al., 2010); this allows the X-ray signal to be mapped to material density. Images are assigned discrete digital grey values (0-255) according to the material density, represented by voxels: pixels in 3-dimensional space (x, y, z coordinates). Using the 3-D image volume graphics package, VGStudio, each sample volume was reconstructed using a threshold procedure to derive an isosurface to define material boundaries. The isosurface was manually derived for each sample to find the best fit to the real surface area and define volumes of solid space (white voxels) and background (black voxels). Inversion of the grey scale of the solid material within each sample isolated the lowest densities - the empty pores (vesicles) - and permitted the accurate determination of the volume, and geometry, of void spaces, in each of the lava samples. The average voxel resolution for the technique, using 37 mm diameter cores, is ~1μm. Values for porosity, derived from CT data, are comparable to connected-porosity values determined from traditional saturation techniques.

Threshold segregated images were extracted from VG Studio as image stacks, and imported to Blob3D (Ketcham, 2005) and Quant3D (Ketcham and Ryan, 2004 for 3-D pore analysis. Blob3D provides a series of manual methods to segregate CT data, and to separate

objects based on a user-defined protocol, which can then be measured for size, intersection, and orientations. The software can also be used to create a best fit ellipsoid, from which we have extracted major, intermediate, and minor axis data (see supplementary files for full details). Pore-shape fabric analysis was conducted on segmented sample core data using Quant3D (Figure 3). Various methods can be applied to the CT data set, including the star volume distribution (SVD: Cruz-Orive et al., 1992), the mean intercept length (MIL: Harrigan and Mann, 1984), and the star length distribution (SLD; Smit et al., 1998). Of these, SLD is the most applicable to 3-D pore shape characterisation; SLD places a series of points within the pores, from which lines are projected outward with a uniform orientation distribution. The length of lines is measured between the original point to the material boundary (i.e. the pore wall); line intersections are used as orientations for directional analysis, and plot as 3-D rose diagrams. SVD is similar but projects lines as infinitesimal cones; the *star volume* is the volume that has direct line of sight from the point of origin. For complex irregular objects, as in the case of natural pores that exhibit internal corners, the pore extremities are obscured, and the star volume may be underestimated in certain directions. MIL projects lines across the sample, but unlike SLD, lines cross multiple material boundaries. As such MIL measures the line length within the pores and the solid rock; results are strongly affected by material distribution, in particular the thickness of solid rock separating pores.

Analyses were conducted using the SLD method for the entire sample core (Figure 3A, 3C, 3E), and for representative individual pores extracted from the sample volume (Figure 3B, 3D, 3F). The main data visualisation output is a 3-D rose diagram, which are displayed to show ellipsoid diameter values divided by the maximum diameter, such that the maximum display value is 1.0; absolute values range between 0.0-1.0. In the case of individual pore analyses, the minimum displayed value is therefore representative of the pore aspect ratio (i.e. c/a: indicated on the colour bars as S, and referring to plots in Figure 3B,D,F). For the full sample volume, the minimum displayed value is the mean aspect ratio for the analysed volume (indicated on the colour bars as V, and referring to plots in Figure

3A,C,E); the rose plot is therefore representative of a preferred shape orientation within the sample.

2.3. Experimental rock deformation

To experimentally simulate near-surface conditions for fracture nucleation and propagation, the unconfined compressive strength (UCS) was measured for 42 samples that represent the 3 main zones of a lava: 12 from the top zone; 4 from the core zone; and 22 from the basal zone. UCS tests were conducted on oven-dried cylindrical cores with a diameter of 37 mm, and tests were performed in accordance with the ISRM suggested methodology (Bieniawski and Bernede, 1979b; Fairhurst and Hudson, 1999). The test apparatus is an MTS 815 servo-controlled, hydraulic rock mechanics testing system, with a 4600 kN loading frame. Samples were taken to failure at a constant strain rate of 5 $x10^{-6}$ sec, with axial and circumferential strain measured throughout experiments. To identify and characterise mechanical anisotropy in the lava, samples were cored and tested in two orthogonal orientations relative to the measured pore shape: (1) a vertical core, oriented normal to bedding, and (2) a horizontal core, oriented parallel to bedding.

3. Results

3.1. CT volume analysis

Pore shape analysis using Quant3D confirms our field characterisation that pores in the studied lavas are not spherical (Figure 3). Individual pores in the top and core zones typically have aspect ratios between 0.60-1.00 (e.g., Figure 3B, 3D). Individual pores in the basal zone are a mixture of large (>5 mm^3) oblate geometries with aspect ratios typically between 0.10-0.40 (e.g., Figure 3F), and smaller (typically <<5 mm^3) pores with lower aspect ratios in the range 0.41-0.80. Large oblate pores in the basal zone are generally well-aligned sub-horizontally (Figure 3E); the contribution of smaller pores with aspect ratios >0.40 has the effect of increasing the mean aspect ratio for basal zone samples (e.g., Fig. 3E: mean aspect

ratio of 0.54). Although pores in the top and core zones are non-spherical (e.g., Fig. 3B,D), the pore long axes show no preferred orientation, giving a mean aspect ratio of ~0.85 in both sample sets (Figure 3A, 3C).

3.2. Uniaxial Compressive Strength

UCS results highlight a distinctive mechanical anisotropy through the lava (Figure 1A; Figure 4A, 4B; Table 1). Each test resulted in an extension to extensional shear fracture along the long axis of the sample (Figure 4C-F), with a principal failure plane forming an acute angle (~15-30°) with the applied maximum compressive stress (σ_1, where $\sigma_1 \geq \sigma_2 \geq \sigma_3$; here compressive stress is reckoned positive). Stress-strain curves (Figure 4A, 4B) show no evidence for premature failure on a pre-existing fracture. Sample bulk density ranges from 2.08-2.64 g/cm^3, showing an inverse relationship with porosity (Figure 1B). Inspection of pre-UCS test thin sections indicates that mineralogy is consistent throughout the lava; samples exhibit minor intragranular or crystal boundary fractures – probably related to cooling – but no preferred orientation was recognised.

The lava core has the lowest porosity (12-13%) and is strong and stiff, irrespective of compression direction, with average peak strengths of 91 MPa (*vertical*) and 106 MPa (*horizontal*), and Young's moduli of 17 GPa and 19 GPa, respectively (Figure 4A, 4B; Figure 5A, 5B). Unit tops have the highest porosity (18-31%) and are weaker with average peak strengths of 57 MPa (*vertical*) and 69 MPa (*horizontal*) UCS, with Young's moduli of 19 GPa and 20 GPa respectively (Figure 4A, 4B; Figure 5A, 5B). This is consistent with the broad inverse relationship shown in Figure 1A.

Conversely, unit bases (15-19% porosity) show a large contrast in average strength, ranging from 40 MPa (*vertical*) to 80 MPa (*horizontal*)*;* Young's moduli: 12 and 20 GPa, respectively; Figure 4A, 4B; Figure 5A, 5B). The strength range in the lava base is reduced when separated by orientation. Samples subjected to the equivalent of horizontal compression (i.e. parallel to bedding) have comparable strengths with the lower porosity core, ranging

between ~80-102 MPa, with an additional sub-set between ~60-70 MPa. However, for samples subjected to the equivalent of vertical compression (i.e. normal to bedding), samples show *much lower* compressive strengths of ~16-30 MPa, with a sub-set of values between ~40-60 MPa. Sample porosity in base samples is relatively constant at ~15-19% (Figure 5A), hence porosity - as a scalar quantity - is not responsible for the variation in rock strength.

The variation in compressive strength measured through the lava unit is best represented using the strength anisotropy ratio (traditionally, the maximum measured compressive strength divided by the minimum measured compressive strength (σ_{cmax}/ σ_{cmin}). This ratio quantifies the anisotropy found in rocks and to define the shape of the anisotropy curve on plots of compressive strength and weakness orientation (i.e. the β angle, e.g. Paterson and Wong, 2005; Ramamurthy et al., 1993). Rocks with ratios <2 are considered to be isotropic or minimally anisotropic (e.g. sandstone); rocks with values between 2-4 are classified as moderately anisotropic (e.g. shale); and those with values >4 are classified as highly anisotropic (e.g. fractured sandstone) (Ramamurthy et al., 1993; Al Harthi, 1998). To define a ratio for samples in this study (tested in two orientations only), we compare median values of strength (i.e. maximum median UCS/minimum median UCS) in each orientation to reduce the influence of potential outlier data. Lava top and core samples in this study appear to be relatively isotropic by this definition with strength anisotropy ratios of 1.39 and 1.16, respectively (Figure 5C). In contrast, lava base samples show a ratio approximately twice that for the rest of the unit at ~2; a value similar to ratios for shales, siltstones, and mudstones. Notably, higher anisotropy ratios in the Kilauea lava samples correlate with high aspect ratios for pores derived from CT volume analysis. Samples are weakest in cases where compression (i.e. σ_1) is applied parallel to the pore short axis.

3.3. 2-D numerical modelling

CT volume analysis shows that pores within the lava base have aspect ratios ranging from 0.1-0.4 (Figure 3). Increasing aspect ratio relative to a sphere, produces a directional

dependence of pore wall curvature. Here we isolate the role of pore curvature using numerical simulation based on Eshelby's solution (Eshelby, 1957, 1959). In our models, a single elliptical pore with an aspect ratio of 0.33 is embedded in an infinite, otherwise homogeneous, isotropic linear elastic matrix (Fig. 6; Fig. 7). Remote stresses are applied far from the pore, and the total stress (and strain) fields are calculated on a regular Cartesian grid of points within the matrix (Fig. 6). Matrix stress components were contoured to produce plots of horizontal (σ_{xx}) and vertical (σ_{zz}) normal stress (Figure 6). Our models involve no fluid, and in each case the applied axial stress is 10 MPa. In the case of applied compression (Figs 6c-f and 7c-f), a confining pressure of 0.1 MPa (1 atmosphere) is applied in the horizontal axis, corresponding to a standard unconfined laboratory test. This remote stress configuration is therefore technically biaxial, but for the purposes of description – and comparison to the UCS tests – we will refer to it as uniaxial. Figure 7 shows perturbation stress due to the pore (i.e. the elastic stress field associated with the pore only, removing the remote stress contribution), for the same applied remote stress as in Figure 6.

For an elliptical pore subject to uniaxial tension in the horizontal axis elevated tensile stress is predicted to develop at the pore maximum curvatures, in both σ_{xx} and σ_{zz} axes (Figs 6A,7A, and Figs 6B,7B respectively), hence these are considered to be the likely sites for failure and crack propagation away from the pore. Axisymmetric compression, replicating UCS experimental conditions for the two test orientations, produces fundamental differences from tensile stress models, in terms of the magnitude and the distribution of the stress perturbation. Where vertical compression is applied parallel to the pore long axis (Figures 6C, 6D and 7C,7D), σ_{xx} is only mildly tensile near the pore tip (Figure 7C) and σ_{zz} shows a similar distribution and perturbation to the tension model at the maximum curvatures (Figure 7D). Hence the pore geometry is *relatively* strong under compression compared to tension. Applying a remote vertical compression parallel to the pore short axis, results in pronounced tensile stress amplification at the crack minimum curvature in both σ_{xx} and σ_{zz} (Figures 6E, 6F and 7E,7F). Importantly, the distribution of that tensile stress amplification is much greater

than that experienced in the other models. Such increases in the area over which stress is amplified will increase the potential for interaction between neighbouring pores, or pre-existing flaws, and promote failure at lower externally applied stresses. These simple models support the strength anisotropy observations recorded in UCS tests for flattened pores in the lava base (Figure 4A, 4B), indicating that pore-shape anisotropy is an important, but hitherto undiagnosed control on rock strength.

4. DISCUSSION

We have shown that pore aspect ratio is a fundamental control in rock strength, with samples containing flat pores showing strength anisotropy ratios that are comparable to foliated sedimentary rocks. Samples were cored at orthogonal angles, from a single block, and detailed characterisation at a range of scales shows that mineralogy, density, porosity, and pore distribution are near identical in both orientations; the only variable between core direction is the relative orientation of the pores with respect to the applied load (e.g., cf. Figure 4E, 4F and 7A, 7B).

4.1 Importance of aspect ratio and the distribution of pores

Numerical models that isolate aspect ratio (e.g. Figure 6) show that pore geometry controls the distribution of stress within a sample, affecting the strength of the material. However, the range in peak strengths for lava base samples suggests that pore aspect ratio can operate in conjunction with additional factors. For instance, samples that show very high aspect ratio pores (e.g., sample 5B: the highest mean aspect ratio in the study at 0.32; Figure 8C, 8D) can be stronger than samples with lower aspect ratio pores (e.g., sample 4B, which has a mean aspect ratio of 0.54-0.58: Figure 8A,8B). Sample 5B is stronger in both the vertical and the horizontal orientation. Sample 4B has a higher porosity (~20%) than 5B (~16%), which contributes in part to the strength difference. However, in the vertical samples (bedding normal) the peak strength of 4B is half that of 5B (i.e., 22 MPa, versus 44 MPa respectively);

269 in the horizontal samples (bedding parallel) the peak strength of 4B is ~65% that of 5B (i.e.
270 66 MPa versus 102 MPa respectively); a large drop in strength for only ~4 percentage point
271 difference in porosity. Inspection of the samples highlights that a further variable between
272 samples is the distribution of pores, and in particular, the spatial distribution of large, oblate
273 pores within the sample volume: sample 5B contains a few very large (up to 26 mm diameter;
274 1-3 mm in the short axis), oblate pores, which are separated by 10-15 mm in the direction of
275 the short axis; sample 4B contains a large number of smaller oblate pores (~5-15 mm
276 diameter; ~1-3 mm in the short axis) that are closer in proximity (i.e. ~5 mm). In the pre-
277 failure elastic regime, the induced tensile stress around pores is additive, and will be
278 particularly effective in cases where pore-pore distances are small relative to the pore
279 diameter; this effect is considered to occur even at low sample porosities (~5-10%; Rice,
280 1997). Although sample 5B may show greater tensile stress amplification, the distance
281 between pores may limit the effect of stress field superposition. Conversely, the combination
282 of stress amplification and greater superposition of stress fields in 4B may cause failure at
283 much lower applied stresses. Hence the range in our UCS data may reflect the combination of
284 surface curvature effects and pore-pore distances. Further study is required to isolate these
285 effects - ideally using manufactured samples – but we consider total porosity alone to be
286 insufficient to characterise rock strength.
287
288 **4.2. Implications for the scaling of rock strength tests**
289 The UCS results presented here show a broad correlation with data for porous materials (e.g.,
290 Figure. 1A), including basalt lavas from various volcanic edifices. UCS and triaxial tests for
291 basaltic rock strength typically involve low porosity samples (~1-4%; e.g.,Heap et al., 2009,
292 2010). Such studies involve large, and reproducible datasets for rock strength, making for a
293 statistically defined intact rock strength (e.g., the eponymous Etna basalt). Rock strength for
294 these low porosity samples is very high (>140 MPa), and they probably represent the very
295 strongest part of an individual lava. Intact rock strength and elastic properties determined

296 through experimental characterisation are important parameters that contribute to *rock mass*
297 *strength* (Hoek and Brown, 1980), which also accounts for meso- to macros-scale
298 discontinuities. It is therefore important to recognise that low porosity test results represent an
299 extreme end-member value for intact rock strengths, and using these values may result in
300 overestimation of the rock mass strength. This may have further implications concerning
301 elastic wave propagation and acoustic velocities, given that the low-porosity lava core may
302 represent only a small proportion of a volcanic edifice. Elastic wave velocities for intact rock
303 can be affected by pore geometry (Takei, 2002). However, it is important to note that intact
304 rock properties are not representative of the complex geometrical arrangement of fractured
305 crystalline units and volcaniclastic materials that comprise a volcano flank (e.g. Thomas et
306 al., 2004; Apuani et al., 2005).
307
308 **4.3. Pore aspect ratio: scaling and broader implications**
309 Our UCS results suggest that for a given porosity, samples that exhibit a strong pore shape
310 anisotropy can be stronger and stiffer than samples containing spherical pores (Fig. 5). This
311 has important implications for micromechanical models of porous rock failure, which idealise
312 pores as equant spheres within an elastic medium (e.g. Sammis and Ashby, 1986; Zhu et al.,
313 2010; Wong and Baud, 2012; Baud et al., 2014; Heap et al., 2014). The response of a curved
314 surface to an applied stress has long been of interest in engineering practice, architecture, and
315 material sciences. Recent numerical-based studies have shown that curved surfaces gain
316 substantial strength when they are compressed along their major axis (Lazarus et al., 2012;
317 Vella et al., 2012; see e.g., Figure 4), and the concept is widely applied to account for the
318 apparent strength of convex structures, from micro-biology in the case of eukaryotic cells
319 (Helfer et al., 2001), virus shells (Roos et al., 2010) and seeds (Pearce et al., 2011), to egg
320 shells (Lazarus et al., 2012; Vella et al., 2012) and larger man-made curved surfaces including
321 domes and bridges. The induced strength of curved surfaces scales proportionally to the
322 aspect ratio of the ellipse (Lazarus et al., 2012), such that doubling the size of the ellipse also

323 doubles the load-bearing capability. The variation in our UCS results correlates with pore
324 shape variability and it is useful to simplify this at a scale of individual non-spherical,
325 elliptical pores to consider strength and stiffness as a function of the radius of curvature. The
326 strongest samples have spherical pores, or pores that are oblate with the major axis parallel to
327 the axis of applied compression; in both instances, the radius of curvature is small with
328 respect to the axis of maximum compression. Conversely the weakest samples – by almost an
329 order of magnitude – are those in which pores are oblate and the axis of compression is
330 applied parallel to the short axis; where the radius of curvature is comparatively large. For a
331 given porosity (i.e. ~16%) sample strength can range between ~15-105 MPa, and therefore
332 characterising *pore geometry*, and not just the scalar *porosity*, is critically important when
333 constraining rock sample strength.
334 Our results show that varying aspect ratio of a void can present a stable configuration
335 relative to an applied tectonic stress. On the basis that strength scales proportionally with
336 aspect ratio, this type of geometry-induced strength may provide a mechanism by which it is
337 possible *to maintain open pores or cavities for extended periods of time*. We envisage that
338 this mechanism may operate in a number of : (1) dilational jogs along faults and fractures,
339 which show evidence for gravitational filling, or textures consistent with slow cementation
340 rates (Frenzel and Woodcock, 2014; Roberts and Walker, 2016); (2) dilational jogs in fault
341 systems that act as conduits for fluid flow and ore deposition in hydrothermal systems (e.g.,
342 orogenic gold deposits; Goldfarb et al., 2005); (3) karstic aquifers (Loucks et al., 1999),
343 which undergo progressive compaction after their formation; and (4) subseafloor cavities that
344 can host microbial systems (Holland et al, 2006) as they permit higher fluid flow, facilitating
345 reactions between hydrothermal solutions and cold, oxygenated water necessary for microbial
346 growth (Orcutt and Edwards, 2014). Geometry-induced strength could increase the potential
347 for sites of large and taxonomically diverse communities of microbial life to exist at greater
348 depths and for longer periods. Such deep biospheres have been the focus of recent IODP

drilling with the discovery that a subseafloor microbial reservoir could outsize that of sediments (e.g., Orcutt and Edwards, 2014; Orcutt et al., 2015).

5. CONCLUSIONS

Our study of vesicular basalt, shows that without changing total sample porosity, rocks can have almost an order of magnitude variation in strength, depending on the orientation of the applied compressive stress relative to pore shape. It is therefore critically important to characterize the true geometry of the pore space, including vesicles and cracks. Pore geometry effects have important implications for rock strength in general, in addition to the maintenance of open pore space, which in turn contributes to the long-term maintenance of permeability in the subsurface.

ACKNOWLEDGMENTS

This study was funded via RJW's University of Leicester start-up fund, as part of AAB's PhD project. We thank Don Swanson and Mike Poland at HVO, Hawai'i, for their help and advice during fieldwork planning and sample collection in the Koa'e fault system, and the National Park Service for granting a research permit to collect rock samples. Sergio Vinciguerra is thanked for access to the Rock Mechanics and Physics lab at the British Geological Survey and Audrey Ougier-Simonin is thanked for her help preparing samples and advice during testing.

REFERENCES CITED

1. Ajalloeian, R. & Lashkaripour, G. R. 2000. Strength anisotropies in mudrocks. *Bulletin of Engineering Geology and the Environment,* 59**,** 195-199.
2. Al-Harthi, A. A., Al-Amri, R. M. & Shehata, W. M. 1999. The porosity and engineering properties of vesicular basalt in Saudi Arabia. *Engineering Geology*, 54, 313-320.
3. Apuani, T., Corazzato, C., Cancelli, A. & Tibaldi, A. 2005. Stability of a collapsing volcano

(Stromboli, Italy): Limit equilibrium analysis and numerical modelling. *Journal of Volcanology and Geothermal Research,* 144**,** 191-210.

4. Baud, P., T. Wong, and W. Zhu. 2014. Effects of porosity and crack density on the compressive strength of rocks. *International Journal of Rock Mechanics and Mining Sciences*. **67**: p. 202-211.
5. Bieniawski, Z. T. & Bernede, M. J. 1979b. Suggested Methods for Determining Water Content, Porosity, Density, Absorption and Related Properties and Swelling and Slake-durability Index Properties. Pergamon.
6. Bieniawski, Z. T. & Bernede, M. J. 2007b. Suggested methods for determining the uniaxial compressive strength and deformability of rock materials: Part 1. Suggested method for determining deformability of rock materials in uniaxial compression. In Ulusay, R. and Hudson, J.A. (eds) *The Complete ISRM Suggested Methods for Rock Characterization, Testing and Monitoring: 1974-2006*. Pergamon.
7. Broch, E., 1983, August. Estimation of strength anisotropy using the point-load test. In *International Journal of Rock Mechanics and Mining Sciences & Geomechanics Abstracts* (Vol. 20, No. 4, pp. 181-187). Pergamon.
8. Cruz-Orive, L.M., Karlsson, L.M., Larsen, S.E. and Wainschtein, F., 1992. Characterizing anisotropy: a new concept. *Micron and Microscopica Acta*, *23*(1), pp.75-76.
9. Eshelby, J. D. (1957, August). The determination of the elastic field of an ellipsoidal inclusion, and related problems. In *Proceedings of the Royal Society of London A: Mathematical, Physical and Engineering Sciences* (Vol. 241, No. 1226, pp. 376-396). The Royal Society.
10. Eshelby, J. D. (1959, October). The elastic field outside an ellipsoidal inclusion. In *Proceedings of the Royal Society of London A: Mathematical, Physical and Engineering Sciences* (Vol. 252, No. 1271, pp. 561-569). The Royal Society.
11. Fairhurst, C.E. and J.A. Hudson. 1999. Draft ISRM suggested method for the complete stress-strain curve for intact rock in uniaxial compression. *International Journal of Rock Mechanics and Mining Sciences*. **36**: p. 279-289.

12. Frenzel, M and Woodcock, N.H. 2014. Cockade breccia: product of mineralisation along dilational faults. *Journal of Structural Geology*, 65, 194-206.
13. Goldfarb R.J., Baker, T., Dubé, B., Groves DI, Hart, C.J.R., Gosselin, P. 2005 Distribution, character, and genesis of gold deposits in metamorphic terranes within Society of Economic Geologists. In: Hedenquist JW (eds) *Economic geology 100th anniversary volume*, 407–450.
14. Harrigan, T.P., Mann, R.W., 1984. Characterization of microstructural anisotropy in orthtropic materials using a second rank tensor. Journal of Materials Science 19, 761–767.
15. Heap, M.J., Vinciguerra, S and Meredith, P.G. 2009. The evolution of elastic moduli with increasing crack damage during cyclic stressing of a basalt from Mt. Etna volcano. *Tectonophysics*, 471, 153-160.
16. Heap, M. J., et al. 2010. Elastic moduli evolution and accompanying stress changes with increasing crack damage: implications for stress changes around fault zones and volcanoes during deformation. *Geophysical Journal International* 183(1), 225-236.
17. Heap, M. J., Xu, T and Chen, C.F. 2014. The influence of porosity and vesicle size on the brittle strength of volcanic rocks and magma. *Bulletin of Volcanology,* 76, 9.
18. Helfer, E., Harlepp, S., Bourdieu, L., Robert, J., Mackintosh, F. C. & Chatenay, D. 2001. Buckling of Actin-Coated Membranes under Application of a Local Force. *Physical Review Letters,* 87.
19. Hoek and Brown, 1980
20. Holland, M., Urai, J.L and Martel, S. 2006. The internal structure of fault zones in basaltic sequences. *Earth and Planetary Science Letters*, 248, 301-315.
21. Hon, K., Kauahikaua, J. P., Denlinger, R. P. & Mackay, K. 1994. Emplacement and inflation of pahoehoe sheet flows: observations and measurements of active lava flows in Kilauea Volcano, Hawaii. *Geological Society of America Bulletin,* 106**,** 353-370.
22. Karakul, H., Ulusay, R. & Isik, N. S. 2010. Empirical models and numerical analysis for assessing strength anisotropy based on block punch index and uniaxial compression tests. *International*

Journal of Rock Mechanics and Mining Sciences, 47**,** 657-665.

23. Ketcham, R.A. and Ryan, T.M., 2004. Quantification and visualization of anisotropy in trabecular bone. *Journal of Microscopy*, *213*(2), pp.158-171.

24. Ketcham, R.A., 2005. Three-dimensional grain fabric measurements using high-resolution X-ray computed tomography. *Journal of Structural Geology*, *27*(7), pp.1217-1228.

25. Lazarus, A., Florijn, H. C. B. & Reis, P. M. 2012. Geometry-Induced Rigidity in Nonspherical Pressurized Elastic Shells. *Physical Review Letters,* 109.

26. Leguillon, D. & Piat, R. 2008. Fracture of porous materials – Influence of the pore size. *Engineering Fracture Mechanics*, 75, 1840-1853.

27. Lian, C., Zhuge, Y and Beecham, S. 2011. The relationship between porosity and strength for porous concrete. *Construction and Building Materials* 25, 11, 4294-4298.

28. Lin, G. & Okubo, P. G. 2016. A large refined catalog of earthquake relocations and focal mechanisms for the Island of Hawai‘i and its seismotectonic implications. *Journal of Geophysical Research: Solid Earth*.

29. Loucks, R. G., Mescher, P. K. & Mcmechan, G. A. 2004. Three-dimensional architecture of a coalesced, collaped paleocave system in the Lower Ordovician Ellenbuger Group, central Texas. *AAPG Bulletin,* 88**,** 545-564.

30. Meille, S., Lombardi, M., Chevalier, J and Montanaro, L. 2012. Mechanical properties of porous ceramics in compression: On the transition between elastic, brittle, and cellular behavior. *Journal of the European Ceramic Society*, 32, 15, 3959-3967.

31. Orcutt, B. N., Sylvan, J. B., Rogers, D. R., Delaney, J., Lee, R. W. & Girguis, P. R. 2015. Carbon fixation by basalt-hosted microbial communities. *Front Microbiol,* 6**,** 904.

32. Orcutt, B.N and Edwards, K.J, 2014. Life in the ocean crust: lessons from subseafloor laboratories. In: *Earth and life processes discovered from subseafloor environments*. Eds. Stein, R., Blackman, D.K., Inagaki, F. and Larsen, H.C. *Developments in Marine Geology*, Vol. 7.

33. Palchik, V. 1999. Technical note: Influence of porosity and elastic modulus on uniaxial

458 compressive strength in soft brittle porous sandstones. *Rock Mechanics and Rock Engineering*, 32**,**
459 4, 303-309.
460 34. Paterson, M.S and Wong, T.F. 2005. *Experimental rock deformation – the brittle field*. 2nd
461 Edition. Springer-Verlag, New York.
462 35. Pearce, S. P., King, J. R. & Holdsworth, M. J. 2011. Axisymmetric indentation of curved elastic
463 membranes by a convex rigid indenter. *Int J Non Linear Mech,* 46**,** 1128-1138.
464 36. Ramamurthy, T., Venkatappa, R. & Singh, J. 1993. Engineering behaviour of phyllites.
465 *Engineering Geology,* 33**,** 209-225.
466 37. Rice, R. W. 1997. Limitations of pore-stress concentrations on the mechanical properties of porous
467 materials. *Journal of Materials Science,* 32**,** 4731-4736.
468 38. Rice, R. W. 1998. *Porosity of Ceramics: Properties and Applications*, New York, Marcel
469 Dekker, Inc.
470 39. Roberts, N. M. W. & Walker, R. J. 2016. U-Pb geochronology of calcite-mineralized faults:
471 Absolute timing of rift-related fault events on the northeast Atlantic margin. *Geology***,** G37868.1.
472 40. Roche, R. C., Abel, R. A., Johnson, K. G. & Perry, C. T. 2010. Quantification of porosity in
473 *Acropora pulchra* (Brook 1891) using X-ray micro-computed tomography techniques. *Journal of*
474 *Experimental Marine Biology and Ecology,* 396**,** 1-9.
475 41. Roos, W.H., Bruinsma, R and Wuite, G.J.L. 2010. Physical virology. *Nature Physics*, Vol.
476 6.
477 42. Sabatakakis, N., Koukis, G., Tsiambaos and Papanakli, S.. 2008. Index properties and
478 strength variation controlled by microstructure for sedimentary rocks. *Engineering*
479 *Geology*, 97, 1-2, 80-90.
480 43. Sammis, C. G. & Ashby, M. F. 1986. The failure of brittle porous solids under compressive stress.
481 *Acta Metallurgica,* 34**,** 511-526.
482 44. Saroglou, H. and Tsiambaos, G., 2008. A modified Hoek–Brown failure criterion for
483 anisotropic intact rock. *International Journal of Rock Mechanics and Mining*
484 *Sciences*, *45*(2), pp.223-234.

45. Schaefer, L., Kendrick, J.E., Oommen, T., Lavallee, Y and Chigna, G. 2015 Geomechanical rock propeties of a basaltic volcano. *Frontiers in Earth Science*, Vol. 3, Article 29.
46. Sibson, R. H. 1985. A note on fault reactivation. *Journal of Structural Geology,* 7**,** 751-754.
47. Smit, T.H., Schneider, E. and Odgaard, A., 1998. Star length distribution: a volume-based concept for the characterization of structural anisotropy.*Journal of microscopy*, *191*, pp.249-257.
48. Takei, 2002
49. Thomas, M. E., Petford, N. & Bromhead, E. N. 2004. Volcanic rock-mass properties from Snowdonia and Tenerife: implications for volcano edifice strength. *Journal of the Geological Society, London,* 161**,** 939-946.
50. Vella, D., Ajdari, A., Vaziri, A. & Boudaoud, A. 2012. Indentation of Ellipsoidal and Cylindrical Elastic Shells. *Physical Review Letters,* 109.
51. Wong, T. & Baud, P. 2012. The brittle-ductile transition in porous rock: A review. *Journal of Structural Geology,* 44**,** 25-53.
52. Zhu, W., P. Baud, and T. Wong, Micromechanics of cataclastic pore collapse in limestone. 2010. *Journal of Geophysical Research*. **115** (B4).

FIGURES

Figure 1. The relationship between pore fraction and the strength of porous materials. (A) Porosity versus strength. Grey box highlights experimental data for this study. (B) Plot of dry density against porosity (this study) shows a linear inverse relationship.

Figure 2. (A) Simplified structural elements map of Kilauea volcano south flank, showing the study sample site on the Kulanaokuaiki fault, part of the Koa'e fault system (KFS). ERZ: East Rift Zone. SWRZ: Southwest Rift Zone. HFS: Hilina Fault System. Inset shows relative position of A, on the south coast of Big Island, Hawaii. (B) View looking south onto the Kulanaokuaiki fault footwall scarp, showing vertical thickness variations and lateral continuity of individual pahoehoe type lavas.

Figure 3. CT scans and 3-D rose plots for vesicles within lava samples, showing full sample data (A,C,E) and representative single vesicle data (B,D,F). Samples were cored normal to bedding. Peak strength and porosity values are for the displayed samples. Colour bars highlight normalised aspect ratios for the single vesicle data (S) and for the entire volume (V). Rose plots show a 3-D oblique view, and views along three orthogonal axes, x, y, and z; note that the bright patch (white) relates to the model illumination. The z-axis represents the direction of applied compression in UCS tests. The x- and y-axes are arbitrary directions orthogonal to compression for reference between the CT scan and the rose plots.

Figure 4. Axial strain results for samples cored (A) vertically (bedding-normal), and (B) horizontally (bedding-parallel). Note the very low strengths for vertically cored lava base samples. (C-F) Examples of pre- and post-failure samples used for UCS testing. Major fractures are highlighted by yellow dashed lines. Cylindrical core samples had diameters of 37 mm and lengths of 80 mm.

Figure 5. Summary of experimental UCS results. (A) UCS versus porosity. (B) Young's modulus versus porosity. (C) Comparison of strength anisotropy ratios for samples tested in this study (black) and other crystalline and clastic rock types (greys).

Figure 6. 2D elastic field models for elliptical pores under uniaxial tension and compression, showing total stress within the solid matrix. **(A,C,E)** Total normal stress parallel to the x-axis (σ_{xx}) and (B,D,F) total normal stress parallel to the z-axis (σ_{zz}). A and B show total normal stress induced during uniaxial tension (10 MPa), applied along the x-axis. C and D show the total normal stress induced by applying 10 MPa compressive stress parallel to the ellipse long-axis. E and F show the total normal stress induced by applying 10 MPa compressive stress parallel to the ellipse short-axis. Note that in C-F, a nominal 0.1 MPa is applied to the x-axis to represent atmospheric pressure, as a comparison to experimental UCS tests.

Figure 7. 2D elastic field models for an elliptical pore under uniaxial tension and compression, showing only the pore-induced stress perturbation within the solid matrix (stress amplification due to the presence of the pore). **(A,C,E)** The σ_{xx} perturbation and (B,D,F) the σ_{zz} perturbation. A and B show the normal stress perturbation induced during uniaxial tension (10 MPa), applied along the x-axis. C and D show the normal stress perturbation induced by applying 10 MPa compressive stress parallel to the ellipse long-axis. E and F show the normal stress perturbation induced by applying 10 MPa compressive stress parallel to the ellipse short-axis. Note that in C-F, a nominal 0.1 MPa is applied to the x-axis to represent atmospheric pressure, as a comparison to experimental UCS tests.

Figure 8. CT scans and 3-D rose plots for vesicles within lava base samples 4B and 5B, showing full sample data (A,C) and representative single vesicle data (B,D). Samples were cored parallel to bedding. Peak strength and porosity values are for the displayed samples. Colour bars highlight normalised aspect ratios for the single vesicle data (S) and for the entire volume (V). Note that the bright patch (white) relates to the model illumination. The z-axis represents the direction of applied compression in UCS tests. The x- and y-axes are arbitrary directions orthogonal to compression for reference between the CT scan and the rose plots.

Supplementary File

Data exported from BLOB-3D micro-CT analysis for a selection of Base, Core, and Top samples in horizontal and vertical sample-core orientations. Plots for the data include the Corey Shape Factor, which measures pore sphericity; the K parameter, which defines the object shape between oblate, plane strain, and prolate ellipsoids; and the Flinn plot, which shows the intensity of the K-parameter shape.

Lava component		Bulk density (g/m^3)	Effective porosity (%)	Strength (MPa)			Young's Modulus (GPa)			Strength Anisotropy Ratio	
				Peak	Mean	Median	*E*	Mean	Median	Median	Mean
Upper flow top	H	2.13	28.20	63.32	63.00	63.32	21.25	21.93	21.25	1.17	1.07
	H	2.10	30.45	66.78			25.72				
	H	2.09	30.09	58.90			18.81				
	V	2.09	29.36	48.81	58.99	54.18	22.04	22.95	22.07		
	V	2.19	22.41	82.30			26.46				
	V	2.19	23.40	45.32			21.19				
	V	2.08	30.81	59.54			22.10				
Lower flow top	H	2.45	17.79	78.45	75.35	75.35	18.90	18.28	18.28	1.39	1.37
	H	2.42	17.97	72.24			17.65				
	V	2.21	25.93	42.38	55.01	55.01	15.20	15.86	15.86		
	V	2.35	21.52	67.63			16.51				
Flow core	H	2.64	12.52	106.04	106.04	106.04	18.51	18.51	18.51	1.16	1.17
	V	2.63	13.19	91.14	90.86	91.14	17.14	16.88	17.14		
	V	2.63	13.26	84.10			15.53				
	V	2.63	12.18	97.35			17.96				
Flow base	H	2.51	16.92	59.67	81.12	78.11	16.10	20.19	20.00	1.81	2.04
	H	2.56	15.81	67.25			18.00				
	H	2.44	19.60	66.40			14.90				
	H	2.56	15.18	78.11			17.90				
	H	2.48	17.46	61.79			12.90				
	H	2.53	14.95	99.37			24.10				
	H	2.52	16.09	102.81			27.50				
	H	2.47	17.72	99.52			25.20				
	H	2.44	12.35	90.11			21.50				
	H	2.44	16.59	75.76			20.00				
	H	2.50	16.81	91.54			24.00				
	V	2.53	15.99	15.83	39.83	43.20	5.40	11.60	12.20		
	V	2.47	18.67	28.85			7.70				
	V	2.46	19.12	21.84			6.64				
	V	2.51	15.66	43.99			10.40				
	V	2.50	16.42	47.08			11.70				
	V	2.53	15.89	51.78			13.60				
	V	2.47	17.83	48.80			11.50				
	V	2.50	16.94	44.39			12.70				
	V	2.52	16.13	39.87			12.80				
	V	2.50	14.92	61.94			17.20				
	V	2.51	15.08	31.23			14.30				
	V	2.50	17.03	42.41			15.20				

563 **Table 1.** Summary of sample physical and mechanical properties. Lava components are listed
564 for vertical cores (V) and horizontal cores (H). Strength aspect ratio is the maximum divided
565 by the minimum value for the *median* values and the *mean* values.

Figure 1
W: 188 mm
H: 115 mm

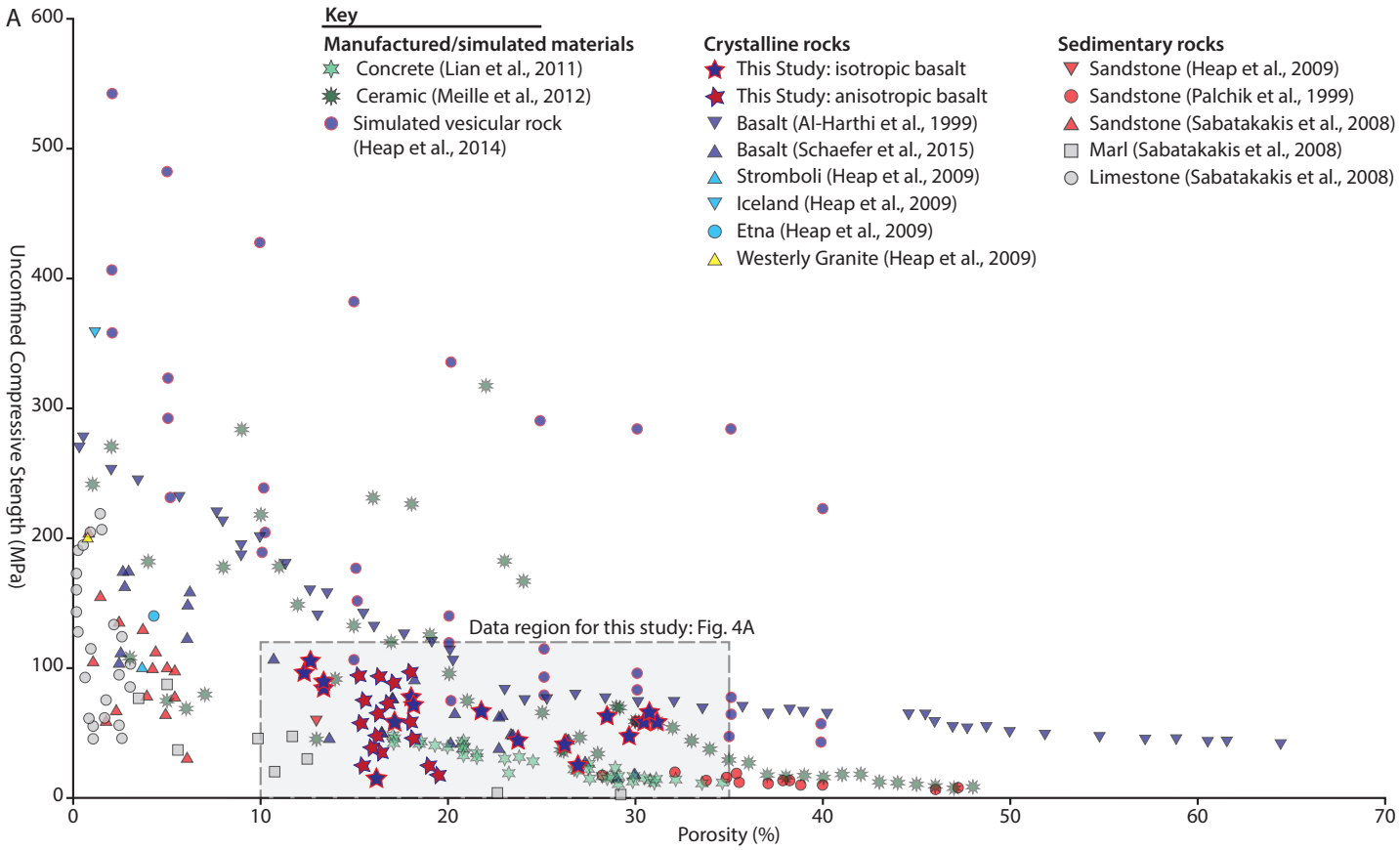

Figure 2
W: 90 mm
H: 107 mm

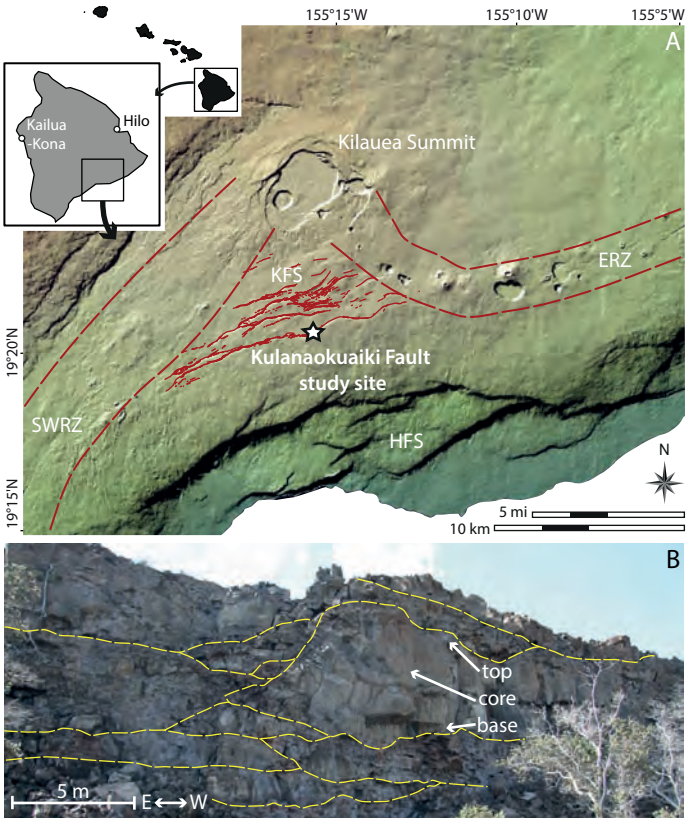

Figure 3
W: 190 mm
H: 208 mm
(full page width)

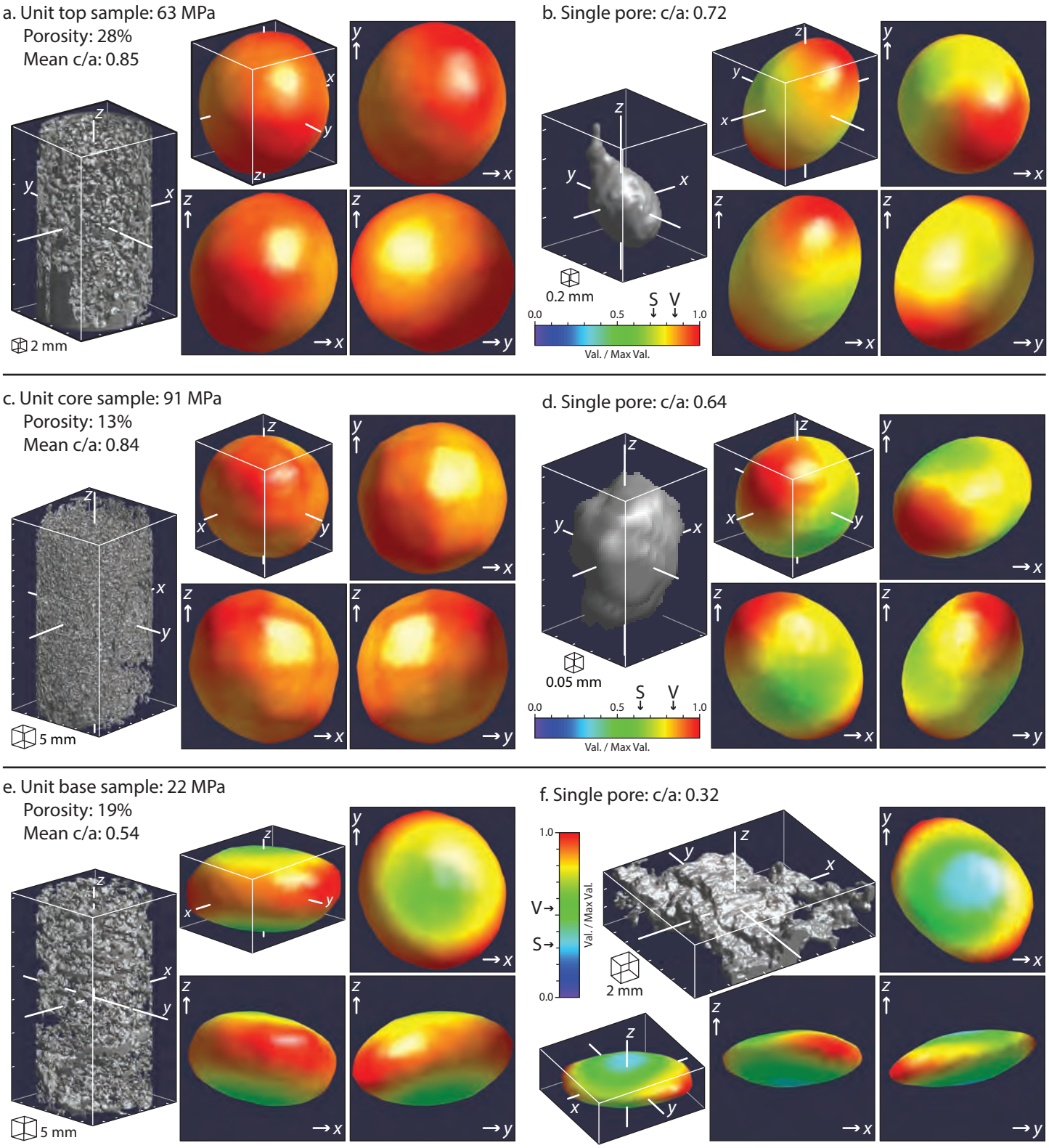

Figure 4
W: 186 mm
H: 182 mm
(full page width)

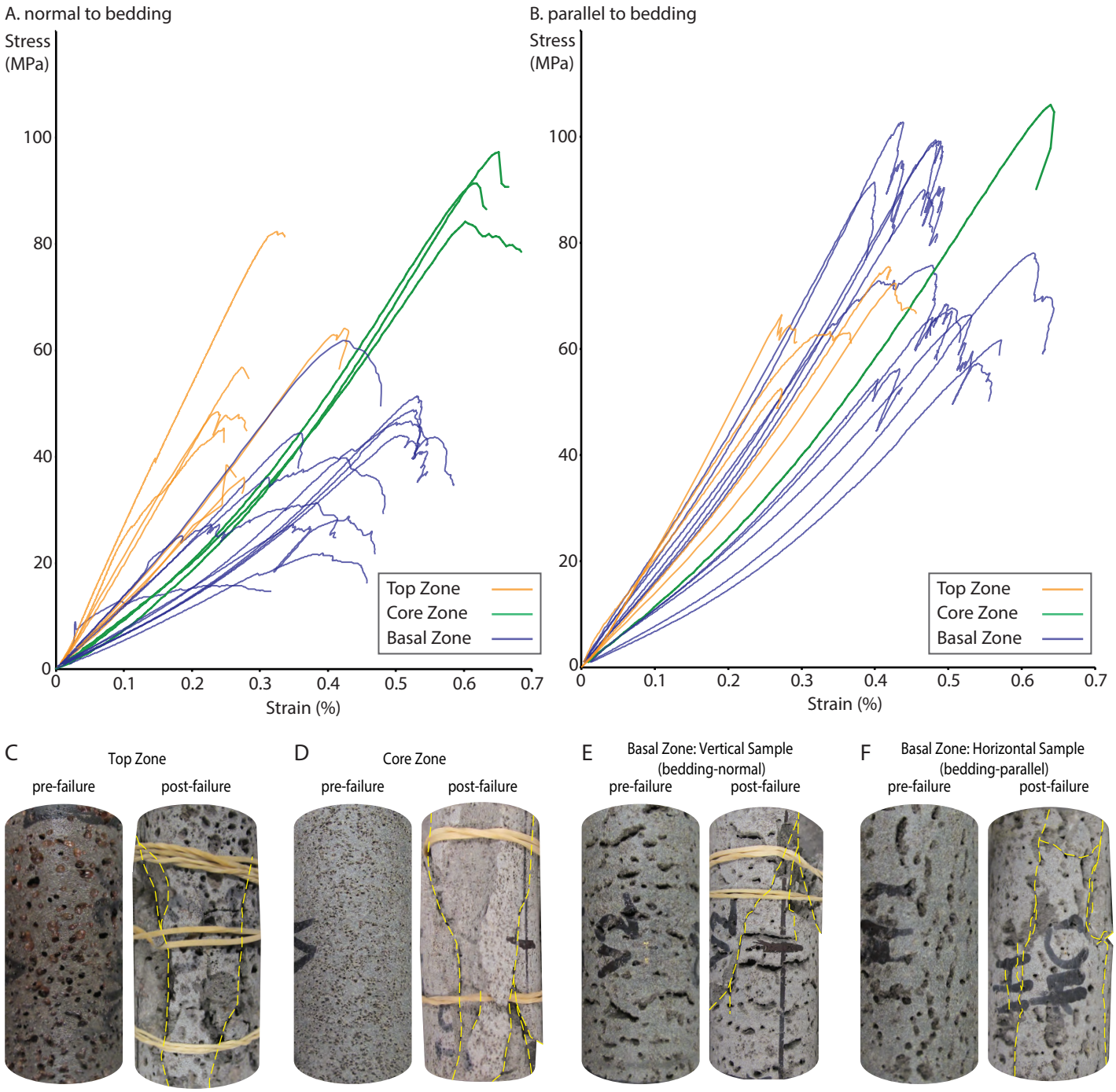

Figure 5
W: 89 mm
H: 202 mm
(single column)

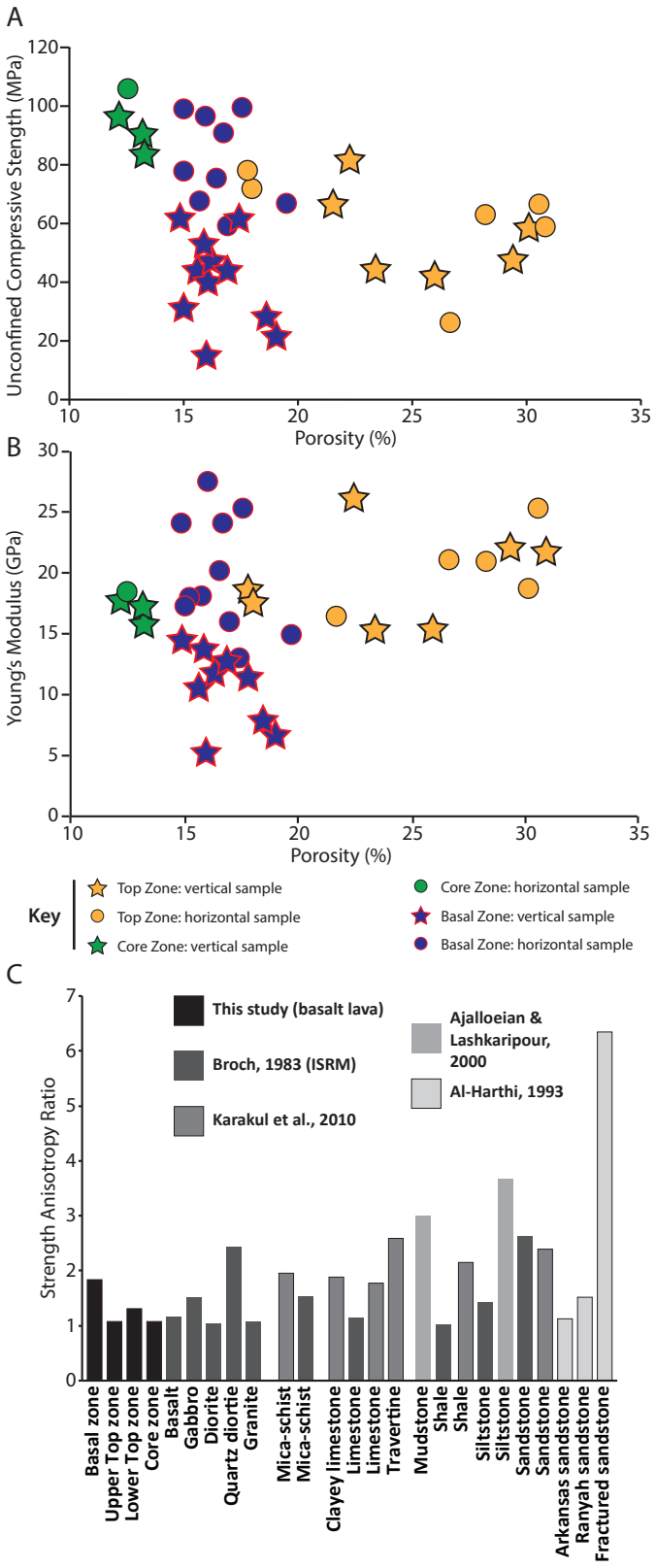

Figure 6
W: 190 mm
H: 154 mm
(full page width)

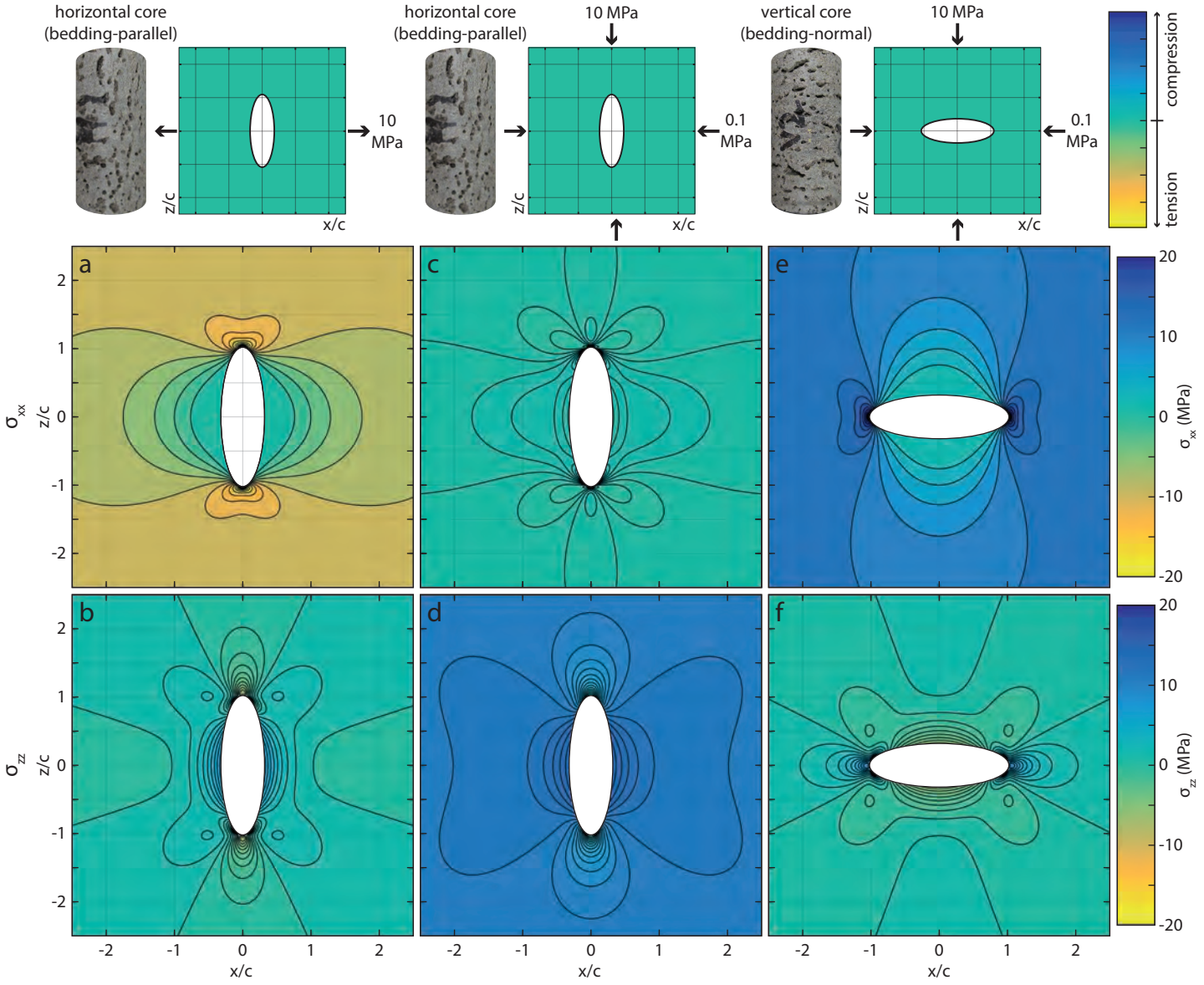

Figure 7
W: 190 mm
H: 154 mm
(full page width)

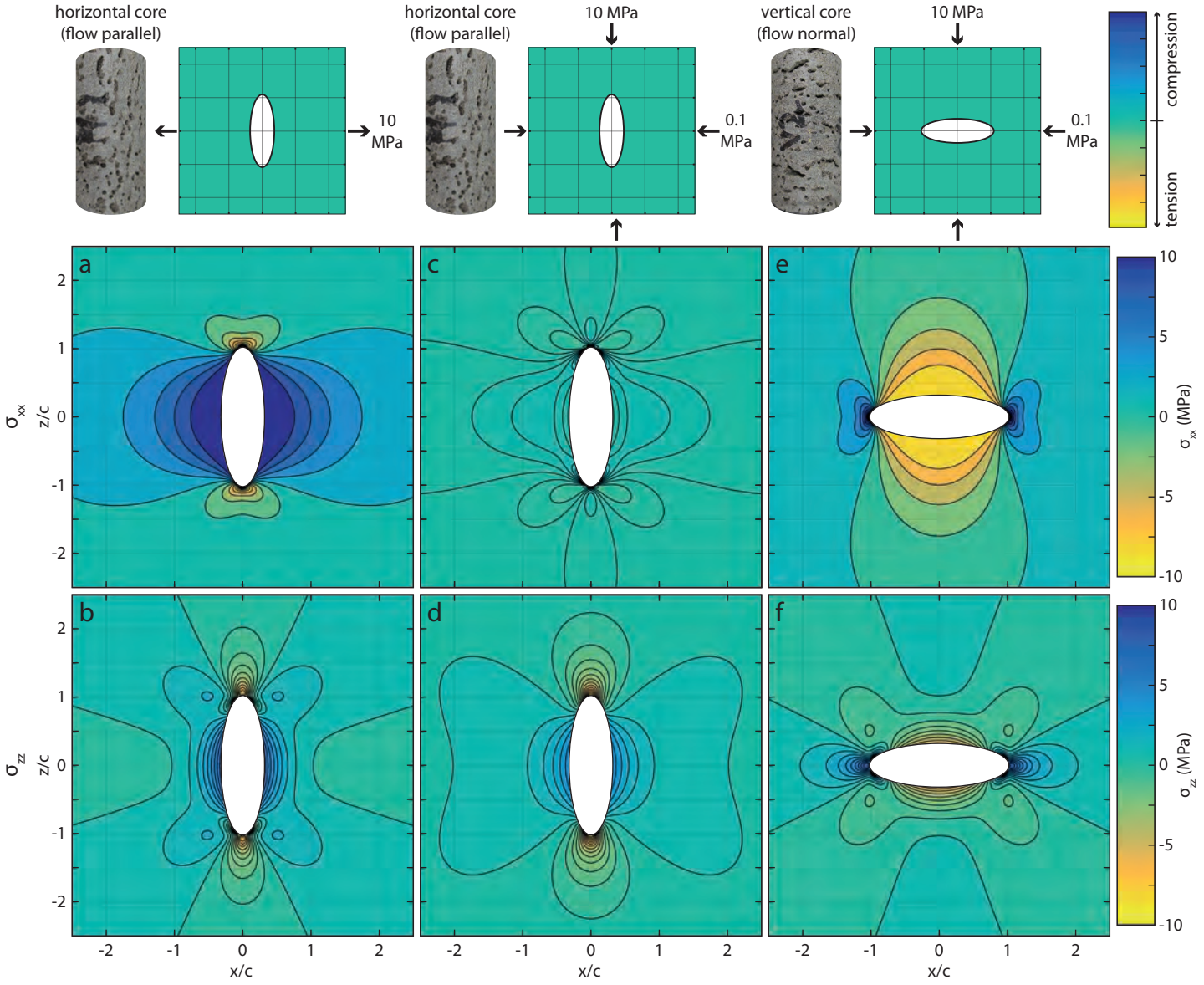

Figure 7
W: 190 mm
H: 137 mm
(full page width)